

Cite this: *Nanoscale*, 2024, **16**, 15141

A molecular dynamics study on the ion-mediated self-assembly of monolayer-protected nanoclusters†

Vikas Tiwari,  Anushna Bhattacharyya and Tarak Karmakar  *

We studied the effects of metal and molecular cations on the aggregation of atomically precise monolayer-protected nanoclusters (MPCs) in an explicit solvent using atomistic molecular dynamics simulations. While divalent cations such as Zn^{2+} and Cd^{2+} promote aggregation by forming ligand–cation–ligand bridges between the MPCs, molecular cations such as tetraethylammonium and cholinium inhibit their aggregation by getting adsorbed into the MPC's ligand shell and reducing the ligand's motion. Here, we studied the aggregation of $\text{Au}_{25}(\text{SR})_{18}$ nanoclusters with two types of ligands, *para*-mercaptobenzoic acid and D -penicillamine, as prototypical examples.

Received 12th June 2024,
Accepted 15th July 2024

DOI: 10.1039/d4nr02427c

rsc.li/nanoscale

1 Introduction

Atomically precise monolayer-protected metal nanoclusters (MPCs), an emerging class of nanometer-sized (<3 nm) molecules having a metal core encircled by a layer of ligands, have redefined the realm of polydisperse nanoparticles.^{1,2} The well-defined metal core and the monolayer of ligands give rise to the distinctive structural features and properties of MPCs.^{3–6} Crucial possibilities for multiple domains arise from the substantial changes that occur to different physicochemical characteristics of MPCs when they undergo aggregation.^{7–10} Among the potential applications are the fabrication of nanodevices¹¹ and nanomaterials,¹² as well as the modification or enhancement of their optical^{13,14} or magnetic behavior.^{15,16}

The exploration of nanocluster (NC) aggregation has emerged as a focal point of interest within the nanomaterials community.^{17–24} This attention is primarily fueled by the recognition that aggregation induces significant alterations in the physicochemical properties of metal NCs when compared to their dispersed state.^{25–27} Among the myriad of properties exhibited by these NCs, photoluminescence (PL) holds particular importance and can be tuned through various strategies. Notably, aggregation-induced emission (AIE)²⁸ has garnered attention due to its remarkable ability to enhance the photoluminescence of metal NCs, resulting in exceptionally high quantum yields.^{25,29–33} AIE involves the implementation of cation-mediated aggregation of MPCs protected with negatively

charged ligand head groups such as carboxylates. In this approach, the aggregation of MPCs is stimulated by introducing oppositely charged species into the solution. The formation of aggregates is facilitated by strong electrostatic interactions between the negatively charged (polar) ligands of the MPCs and metal cations in the solution, leading to the facile formation of aggregates.

Bain *et al.* recently reported that the addition of a divalent Zn^{2+} ion caused the NCs to aggregate, resulting in a significant PL boost of Au NCs.³⁴ Yao *et al.* employed a straightforward and versatile technique that involved carefully generating electrostatic interactions between negatively charged ligands and divalent cations (such as Zn^{2+} and Cd^{2+}).³⁵ In the presence of the counter ion Zn^{2+} , Kuppan and his group studied the self-assembly of highly ordered, one-dimensional green emitting NCs from randomly aggregated Au NCs.³⁶ Zn^{2+} -induced gold cluster aggregation was also employed to develop an electro-chemiluminescence (ECL) biosensor with extraordinary sensitivity for microRNA-21 detection, using it as a high-efficiency ECL emitter.³⁷ Qu *et al.* observed a noticeable increase in glutathione-AuNC emission enhancement upon the addition of Zn^{2+} and Cd^{2+} in the presence of silicon nanoparticles and thus developed a ratiometric sensor to measure the relevant ions.³⁸ Thus, cations can be used to induce MPC aggregation, and alternatively, cation-induced aggregation may be utilized for the detection of metal ions in solution-sensing applications.

Ion-mediated AIE in MPCs has shown promising applications^{39–41} in various fields, which in turn needs a proper detailed understanding of the aggregation mechanism. An atomistic understanding of the interactions of various types of cations (metal and molecular) with MPC ligands and

Department of Chemistry, Indian Institute of Technology, Delhi, Hauz Khas, New Delhi 110016, India. E-mail: tkarmakar@chemistry.iitd.ac.in

† Electronic supplementary information (ESI) available: Supplementary figures and videos. See DOI: <https://doi.org/10.1039/d4nr02427c>

the mechanism of cation-induced aggregation is crucial for the rational design of ligands for MPC preparation and choosing the MPC–cation combinations.

In this work, we have studied the cation-induced aggregation of $\text{Au}_{25}(\text{SR})_{18}$ NCs with two types of ligands, *para*-mercaptobenzoic acid (*p*MBA), a simple aromatic carboxylate, and *D*-penicillamine (DPA),³⁴ a peptide-based ligand, as prototypical ligands (Fig. 1). Using molecular dynamics (MD) and enhanced sampling simulations, we studied the effects of metal cations Zn^{2+} and Cd^{2+} and molecular cations cholinium (Ch^+) and tetraethylammonium (TEA^+) on the aggregation of MPCs (Fig. 1). Our results show that while Zn^{2+} and Cd^{2+} ions

promote the aggregation of Au-NCs, the bulky molecular cations, Ch^+ and TEA^+ , inhibit the self-assembly.

2 Results and discussion

2.1 Dimerization

Studying dimerization serves as a crucial avenue for comprehending the self-assembly processes of MPCs as it elucidates the pivotal interactions responsible for the formation of self-assembled structures.^{23,24} Hence, a dimeric system was set up using pre-equilibrated monomers of $\text{Au}_{25}(\text{SR})_{18}$ MPCs with two types of ligands: (1) *p*MBA and (2) DPA (Fig. 1). In both the ligands, we chose deprotonated carboxylic acid groups based on experimental results indicating that increased photoluminescence of the nanocluster is observed at a high pH value (8).³⁴ At this pH, all *p*MBA ligands are found to be deprotonated.⁴² Equilibrium MD simulations of these two dimeric systems were performed for 100 ns in the presence of Zn^{2+} ions with a Zn^{2+} to ligand ratio ($R_{[\text{Zn}^{2+}/\text{ligand}]}$) of 1.0, which is selected based on simulations performed at various values of $R_{[\text{Zn}^{2+}/\text{ligand}]}$ (Fig. S1†). Formation of an MPC-dimer was observed in both $\text{Au}_{25}(\text{pMBA})_{18}$ and $\text{Au}_{25}(\text{DPA})_{18}$ systems (Fig. 2a and b). The simulation trajectories were analyzed for MPC's COM–COM distance, and the Au–DPA system showed the formation of a relatively more stable dimer within ~25 ns simulation time, which remained intact throughout the entire simulation. On the other hand, the dimer formed in the Au–*p*MBA system was comparatively less stable, and the back-and-forth transitions between the dimeric and monomeric states were frequently observed, which implies comparable stability between the two states (Fig. 2c). Self-assembly can be induced

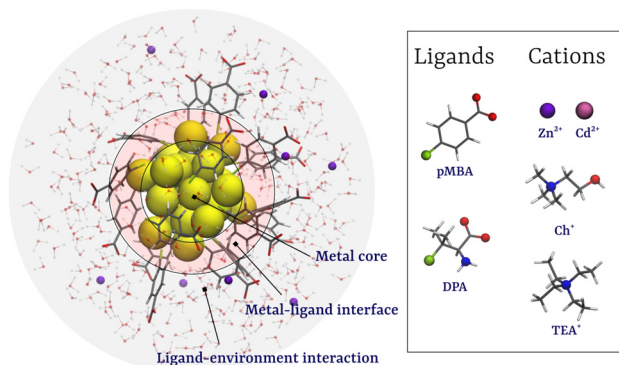


Fig. 1 Representation of an $\text{Au}_{25}(\text{SR})_{18}$ MPC surrounded by the solvent (water) in the presence of cations. Ligands: *para*-mercaptobenzoic acid (*p*MBA) and *D*-penicillamine (DPA), divalent inorganic cations: Zn^{2+} and Cd^{2+} and monovalent molecular cations: cholinium (Ch^+) and tetraethylammonium (TEA^+).



Fig. 2 (a) Snapshot showing the dimer of $\text{Au}_{25}(\text{pMBA})_{18}$ in the presence of Zn^{2+} ions, (b) snapshot showing the dimer of $\text{Au}_{25}(\text{DPA})_{18}$ in the presence of Zn^{2+} ions, (c) MPC's COM–COM distance plotted against the simulation time, (d) coordination number of Zn^{2+} ions between the COM of two MPCs, (e) radial distribution function ($g(r)$) analysis, and (f) root mean square deviation (RMSD) analysis.

in the presence of cations by various driving forces such as electrostatic interactions, van der Waals interactions, dipolar interactions, and metal chelation to attain dimerization in the MPCs. After careful observation of the dimer interface, it was observed that the Zn^{2+} ions interact with the ligands' carboxylate groups *via* a solvation shell forming hydrogen bonds (Fig. 2a) along with the electrostatic interactions. Due to the presence of an additional $-\text{NH}_2$ group in the DPA ligand, an extended hydrogen bond network was observed in the case of the Au-DPA system (Fig. 2b and video S1†). This also led to a higher number of Zn^{2+} at the interface of Au-DPA than in Au-*p*MBA (Fig. 2d). Radial distribution function (RDF) analysis was performed and it confirmed the stronger correlation between Zn and O in Au-DPA compared to that in Au-*p*MBA (Fig. 2e). The main driving force behind the clustering of MPCs is the strong electrostatic attraction between Zn^{2+} and the COO^- group of the ligand as well as the strong hydrogen bond network formed by the hydration shell of the Zn^{2+} ions with the ligands.

The experimental reports on Zn^{2+} -induced Au-MPC self-assembly show an increase in photoluminescence, attributed to the restricted rotation and vibration of ligands of MPCs exerted by electrostatic interactions of Zn^{2+} with the ligands' carboxylate groups. The formation of self-assembly further suppresses the rotation and vibration of ligands, causing an increase in the radiative rate of Zn–Au MPCs while suppressing the nonradiative decay.^{34,35} Hence, to comprehend the effects of Zn^{2+} on the rotation and vibration of ligands, we calculated the root mean square deviations (RMSD) of the ligands present at the dimer interface. A kernel density estimation (KDE) was plotted for the dimeric system with (blue) and without (green) Zn^{2+} ions (Fig. 2f). In the presence of Zn^{2+} ions, a sharp peak centered at around RMSD = 0.1 nm was obtained, whereas in the absence of Zn^{2+} ions, ligand RMSD values spread over a range from 0.5 to 3 nm (Fig. 2f). These results explain the conjecture that Zn^{2+} ions suppress the ligand motions and are in line with experimental observations on the PL enhancement due to cation-mediated MPC aggregation.^{34,35}

To further understand the energetics of Au-DPA MPC dimerization, we carried out a well-tempered metadynamics (WTMetaD) simulation using two collective variables, s_1 , which is the COM–COM distance between the MPCs, and s_2 , which is the interfacial Zn^{2+} coordination number (Fig. S2†). The reweighted free energy surface (FES) is plotted on the s_1 and s_2 variable spaces (Fig. 3). The Au-DPA dimer is stable by ~ 15 kJ mol⁻¹ with a barrier of a few kJ mol⁻¹ for the monomer-to-dimer transition.

Similar results were obtained when Zn^{2+} was replaced by Cd^{2+} , as discussed in the ESI section S5 (Fig. S3 and S4†). The effects of these two cations are comparable, which is not surprising, given that Cd is immediately below Zn in group 12 of the periodic table with a larger ionic radius (of the cation) and similar chemical properties. An interesting observation when comparing the interactions of Zn^{2+} and Cd^{2+} with ligand $-\text{COO}^-$ was on the $g(r)$ plots (Fig. 2e and Fig. S3d†); unlike in



Fig. 3 Free energy profile for the dimerization of $\text{Au}_{25}(\text{DPA})_{18}$ in the presence of Zn^{2+} ions.

the former, in the latter case, we observed a sharp peak at 0.2 nm in $g(r)_{\text{Cd-O}}$ that corresponds to the penetration of a few carboxylate oxygen atoms into the first coordination shell of the Cd^{2+} ions. Free energy calculations using the on-the-fly probability-based enhanced sampling (OPES) method^{43,44} revealed a lower energy barrier for the $-\text{COO}^-$ binding to Cd^{2+} than to Zn^{2+} . Furthermore, Zn^{2+} has another high barrier for entering the double coordinated attachment to the carboxylate ion (see details in section S6 and Fig. S5 and S6 of the ESI†).

2.2 Effect of $R_{[\text{Zn}^{2+}/\text{ligand}]}$ on the self-assembly of Au-DPA

We extended our investigation on the Zn^{2+} -mediated aggregation process and studied the effect of Zn^{2+} concentration on the aggregation propensity. Recently, Yao *et al.*³⁵ reported that with increase in the ratio of Zn^{2+} ions to ligands, $R_{[\text{Zn}^{2+}/\text{ligand}]}$, the aggregation propensity of Au NCs significantly increased. In particular, the size of self-assembled MPCs was observed to be maximum at a charge balance between ligands and Zn^{2+} ions, with $R_{[\text{Zn}^{2+}/\text{ligand}]}$ at around 0.5. Beyond this point, an increase in $R_{[\text{Zn}^{2+}/\text{ligand}]}$ to 1.0 resulted in a decrease in the size of the self-assembled nanoclusters.³⁵ To further investigate this phenomenon, we conducted a series of simulations with 20 randomly dispersed Au-DPA MPCs and monitored the self-assembly process. Simulations were performed with $R_{[\text{Zn}^{2+}/\text{ligand}]} = 0.3, 0.5,$ and 1.0 . The evolution of the aggregation with the simulation time is shown in Fig. S7 and Video S2.† At $R_{[\text{Zn}^{2+}/\text{ligand}]} = 0.3$, small aggregates comprising no more than 3 MPCs were observed (Fig. 4a). Zn^{2+} ions act as bridges between the clusters, promoting aggregation. However, due to a smaller number of Zn^{2+} ions compared to those of ligands, the repulsion between the negatively charged ligands dominates over the bridging effect of Zn^{2+} ions. Whereas, at $R_{[\text{Zn}^{2+}/\text{ligand}]} = 0.5$, a charge balance between Zn^{2+} ions and ligands leads to strong inter-cluster interactions mediated by the Zn^{2+} induced bridging effect. This results in the formation of multiple small aggregates containing 5–10 MPC molecules, each at the initial stage of the simulation, which, at a later stage, aggregate to form a large cluster containing 20 MPCs (Fig. 4b).



Fig. 4 Snapshots at 300 ns of simulation with 20 $\text{Au}_{25}(\text{DPA})_{18}$ MPCs with $\text{Zn}^{2+}/\text{ligand}$ ratios of (a) 0.3, (b) 0.5, and (c) 1.0. (d) DFS cluster analysis showing the size of the largest cluster with respect to the simulation time and (e) zoomed-in image of the cluster formed in (b).

Furthermore, increasing $R_{[\text{Zn}^{2+}/\text{ligand}]}$ to 1.0 resulted in the formation of faster local self-assembled structures composed of 4–5 MPCs (Fig. 4c). Interestingly, unlike in the $R_{[\text{Zn}^{2+}/\text{ligand}]} = 0.5$ system, in the $R_{[\text{Zn}^{2+}/\text{ligand}]} = 1$ system, the small clusters did not aggregate to form a large cluster. This can be due to the high salt (ZnCl_2) concentration, causing electrostatic screening of the charged clusters. The Depth-First Search (DFS) clustering algorithm was employed to monitor the evolution of various clusters and calculate the size of the largest cluster (Fig. 4d). These observations complemented the experimental findings,³⁵ further elucidating the role of Zn^{2+} ions in MPC's self-assembly. Similar results were obtained when the simulation was carried out in the presence of Cd^{2+} ions at $R_{[\text{Zn}^{2+}/\text{ligand}]} = 0.5$ (Fig. S7d and S8†).

2.3 Self-assembly inhibition of Au-MPCs in the presence of Ch^+ and TEA^+ ions

In contrast to our findings with divalent cations Zn^{2+} and Cd^{2+} as mediators in the self-assembly process, the quaternary ammonium cations, namely Ch^+ and TEA^+ , inhibit MPC aggregation. The ion-mediated inhibition strategy has multiple applications such as in biomedical imaging and chemosensing.⁴⁵ While simulating a system with two Au-*p*MBA MPCs and Ch^+ ions in water, we discovered that the Ch^+ cations eventually begin to consolidate or freeze on the MPCs' surfaces (Fig. 5a). Apart from the electrostatic interactions, due to the planar nature of *p*MBA ligands, it shows $\text{CH}-\pi$ interactions between the CH bonds of the Ch^+ cation and the benzene ring of *p*MBA ligands (Fig. 5a).⁴⁶ Whereas, in the case of Au-DPA, because of the bulky DPA ligands, which sterically prevent the

cations from approaching closer to MPCs, the ions are restrained from gliding around the MPC's periphery. Hence, Ch^+ ions mainly interact *via* an H-bond with the DPA ligands along with electrostatic attraction (Fig. 5b). The coordination number analysis also shows a higher number of Ch^+ ions present around Au-*p*MBA as compared to Au-DPA (Fig. 5e). Furthermore, the COM-COM distance analysis reveals the presence of only monomers of MPCs in both *p*MBA and DPA (Fig. 5c). The radial distribution function ($g(r)$) analysis indicates a stronger correlation between the nitrogen of Ch^+ and the oxygen atoms of COO^- in *p*MBA compared to the COO^- of DPA (Fig. 5d). In the case of DPA ligands, the $g(r)$ analysis reveals two distinct humps near 0.5 nm, attributed to H-bonding interactions with one of the oxygen atoms of $-\text{COO}^-$. Specifically, the first hump corresponds to the distance between the nitrogen and the oxygen atoms involved in H-bonding (N-O1). In contrast, the second hump corresponds to the distance between the nitrogen atom and the other oxygen atoms of COO^- (N-O2) (Fig. 5d).

Subsequent simulations utilizing TEA^+ cations yielded similar results with Au-*p*MBA. However, with Au-DPA, the bulky nature of TEA^+ ions resulted in very weak interactions with the ligands due to steric hindrance. In contrast to Ch^+ , TEA^+ is unable to form hydrogen bonds with the DPA ligands (Fig. S9†). Also, it shows a negligible correlation in RDF analysis and approximately zero probability for coordination with the nanocluster, which suggests that it exists mostly as non-interacting ions in solution (Fig. S9d and e†). Furthermore, a multimeric system consisting of 20 randomly dispersed Au-DPA MPCs was simulated for 100 ns in the presence of TEA^+

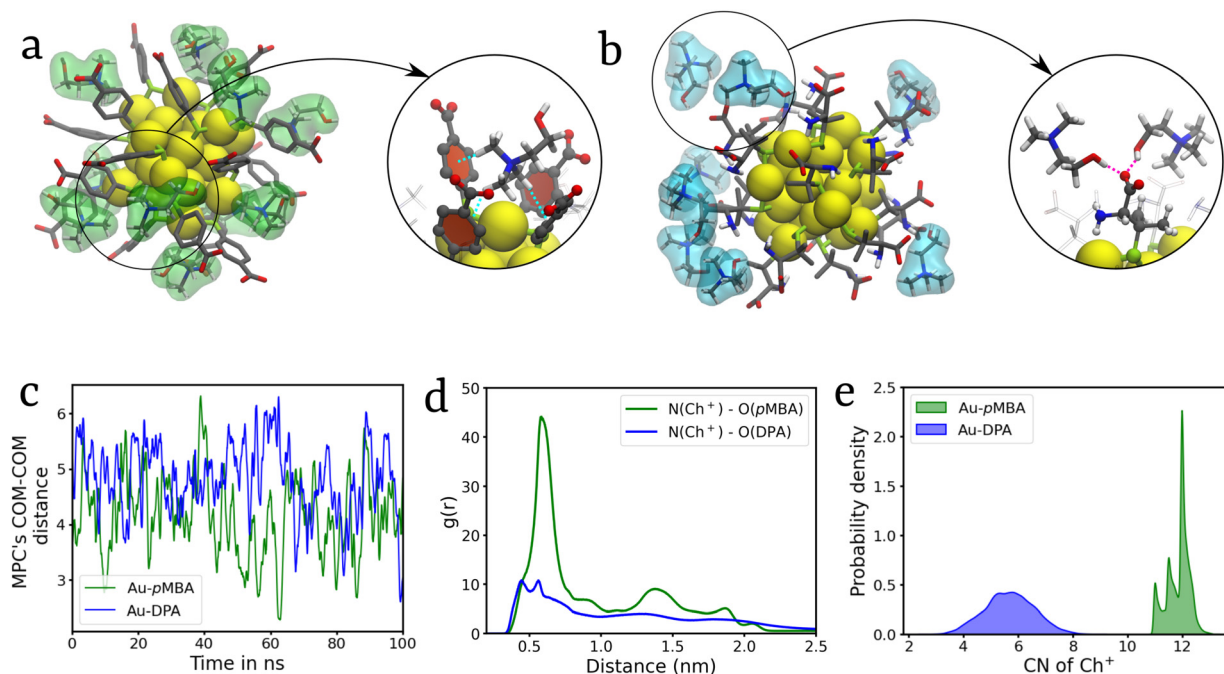


Fig. 5 (a) Univalent cholinium ion (green) interactions with $\text{Au}_{25}(\text{pMBA})_{18}$. (b) Ch^+ interactions with $\text{Au}_{25}(\text{DPA})_{18}$. (c) MPC's COM-COM distance plotted against the simulation time. (d) Radial distribution function. (e) Number of Ch^+ ions which coordinate with $\text{Au}_{25}(\text{SR})_{18}$.

and Ch^+ , and the results observed are consistent with our findings in the case of the dimeric system depicting a strong inhibition of the self-assembly. Cluster analysis further confirms the monomeric dispersion (Fig. S10[†]). Further discussion of these findings can be found in ESI section S8.[†]

3 Conclusions

In summary, our investigation reveals distinct impacts of divalent metal cations and monovalent molecular cations on the behavior of MPCs. While M^{2+} ions (where $\text{M} = \text{Zn}, \text{Cd}$) facilitate the aggregation of MPCs, Ch^+ and TEA^+ ions hinder the self-assembly process. In the dimerization process, M^{2+} ions engage in electrostatic interactions with the negatively charged ligands of MPCs, effectively pulling them together to form dimers. Moreover, the water molecules coordinated around the M^{2+} ions contribute to a robust H-bond network with the ligands, further stabilizing the dimeric structures. Notably, our analysis of $R_{[\text{Zn}^{2+}/\text{ligand}]}$ aligns well with experimental observations, indicating the formation of the largest clusters occurring at $R_{[\text{Zn}^{2+}/\text{ligand}]} = 0.5$, representing the point of charge balance where the total charge on Zn equals the total charge on the ligands. Furthermore, we observed contrasting interactions between Ch^+ and TEA^+ ions with Au-pMBA and Au-DPA. In the case of Au-pMBA, Ch^+ and TEA^+ ions exhibit strong interactions, attributed to both electrostatic forces and $\text{CH}-\pi$ interactions. Conversely, with Au-DPA, Ch^+ ions were found to interact primarily *via* H-bonding. However, the steric hindrance caused by TEA^+ resulted in repulsion dominating

over electrostatic attraction, leading to a weaker correlation between Au-DPA and TEA^+ ions.

4 Methods

4.1 Force field details

The $\text{Au}_{25}(\text{SR})_{18}$ NC structure and topology were generated using the NanoModeler server.^{47,48} The gold-sulfur motifs have bonded and non-bonded terms that were developed according to the work of Pohjolainen *et al.*⁴⁹ and Heinz *et al.*⁵⁰ and implemented in NanoModeler.⁴⁸ The General AMBER Force Field (GAFF)⁵¹ was utilized for MPC ligands and Ch^+ and TEA^+ ions. The TIP3P potential model was used for water molecules. Lennard-Jones (LJ) force field parameters for Cd^{2+} were adapted from the work of Araujo *et al.*⁵²

4.2 System details

The details of the systems simulated in this work are provided in Table 1.

Table 1 System simulated in this work^a

	$\text{Au}_{25}(\text{pMBA})_{18}$	$\text{Au}_{25}(\text{DPA})_{18}$
Zn^{2+}	Dimer	Dimer, multimer
Cd^{2+}	Dimer	Dimer, multimer
Ch^+	Dimer	Dimer, multimer
TEA^+	Dimer	Dimer, multimer

^a The choice of the cations in this study is based on the experimental results reported in ref. 35, 34 and 46.

4.3 Well-tempered metadynamics simulation details

The kinetics and thermodynamics of Au-DPA dimerization in the presence of Zn^{2+} ions were extensively investigated using well-tempered metadynamics simulations.⁵³ Two collective variables were employed for this analysis: s_1 , representing the COM-COM distance between the two MPCs (with only gold atoms considered for calculating the MPCs' COM), and s_2 , indicating the number of Zn^{2+} ions present at the dimeric interface of the MPCs. The calculation of s_2 involved determining the number of coordinated Zn^{2+} ions around the center of COMs of the MPCs (*i.e.*, the interface) within a radial cutoff of 1 nm.

For s_1 , a Gaussian width (σ) of 0.1 nm was chosen, while for s_2 , it was set to 0.5 nm. The initial Gaussian height of 1.0 kJ mol⁻¹ was utilized, along with a bias factor of 5, to explore the free energy landscape of the system effectively. These parameters allowed for a thorough characterization of the dimerization process and its energetics in the presence of Zn^{2+} ions.

Author contributions

The project was conceived and the main conceptual ideas were developed by V.T. and T.K. Computation and analyses were conducted by V.T. and A.B., who also drafted the manuscript and designed the figures. T.K. assisted in interpreting the results and contributed significantly to writing and improving the manuscript. All authors actively participated in discussions regarding the results and contributed to writing the manuscript.

Data availability

All input files required to run the simulations presented in this work can be found in a public GitHub repository (https://github.com/vikast282/Ion_med_self_assembly).

Conflicts of interest

There are no conflicts to declare.

Acknowledgements

V. T. is thankful to the Ministry of Education, Govt. of India for the PMR Fellowship. A. B. acknowledges IIT Delhi for the MTech fellowship. T. K. acknowledges the Science and Engineering Research Board (SERB), New Delhi, India for the Start-up Research Grant (file no. SRG/2022/000969). We also acknowledge IIT Delhi for the Seed Grant. We thank the IIT Delhi HPC facility for computational resources.

References

- R. Jin, C. Zeng, M. Zhou and Y. Chen, *Chem. Rev.*, 2016, **116**, 10346–10413.
- I. Chakraborty and T. Pradeep, *Chem. Rev.*, 2017, **117**, 8208–8271.
- S. Malola and H. Häkkinen, *Nat. Commun.*, 2021, **12**, 2197.
- A. Nag and T. Pradeep, *ACS Nanosci. Au*, 2022, **2**, 160–178.
- M. Bini, V. Tozzini and G. Brancolini, *J. Phys. Chem. B*, 2023, **127**, 8226–8241.
- G. Brancolini, V. M. Rotello and S. Corni, *Int. J. Mol. Sci.*, 2022, **23**, 2368.
- S. Chen, *J. Phys. Chem. B*, 2000, **104**, 663–667.
- A. W. Snow, M. G. Ancona, W. Kruppa, G. G. Jernigan, E. E. Foos and D. Park, *J. Mater. Chem.*, 2002, **12**, 1222–1230.
- Z. Wu, J. Liu, Y. Li, Z. Cheng, T. Li, H. Zhang, Z. Lu and B. Yang, *ACS Nano*, 2015, **9**, 6315–6323.
- J. V. Rival, P. Mymoona, K. M. Lakshmi, Nonappa, T. Pradeep and E. S. Shibu, *Small*, 2021, **17**, 2005718.
- M. Aslam, N. Chaki, J. Sharma and K. Vijayamohan, *Curr. Appl. Phys.*, 2003, **3**, 115–127.
- Z. Wu, Q. Yao, S. Zang and J. Xie, *ACS Mater. Lett.*, 2019, **1**, 237–248.
- M. Cui, Y. Zhao and Q. Song, *TrAC, Trends Anal. Chem.*, 2014, **57**, 73–82.
- R. Jin, *Nanoscale*, 2015, **7**, 1549–1565.
- J. P. Wilcoxon and B. L. Abrams, *Chem. Soc. Rev.*, 2006, **35**, 1162.
- M. Tadic, S. Kralj, M. Jagodic, D. Hanzel and D. Makovec, *Appl. Surf. Sci.*, 2014, **322**, 255–264.
- N. Goswami, K. Zheng and J. Xie, *Nanoscale*, 2014, **6**, 13328–13347.
- Y. Lin, P. Charchar, A. J. Christofferson, M. R. Thomas, N. Todorova, M. M. Mazo, Q. Chen, J. Douth, R. Richardson, I. Yarovsky and M. M. Stevens, *J. Am. Chem. Soc.*, 2018, **140**, 18217–18226.
- Z. Shen, W. Baker, H. Ye and Y. Li, *Nanoscale*, 2019, **11**, 7371–7385.
- M. Vanzan, M. Rosa and S. Corni, *Nanoscale Adv.*, 2020, **2**, 2842–2852.
- S. Dutta, S. Corni and G. Brancolini, *Int. J. Mol. Sci.*, 2021, **22**, 3624.
- W. A. Dar, A. Jana, K. S. Sugi, G. Paramasivam, M. Bodiuzzaman, E. Khatun, A. Som, A. Mahendranath, A. Chakraborty and T. Pradeep, *Chem. Mater.*, 2022, **34**, 4703–4711.
- V. Tiwari and T. Karmakar, *J. Phys. Chem. Lett.*, 2023, **14**, 6686–6694.
- A. Bhattacharyya, V. Tiwari and T. Karmakar, *J. Phys. Chem. Lett.*, 2024, **15**, 687–692.
- S. Maity, D. Bain and A. Patra, *J. Phys. Chem. C*, 2019, **123**, 2506–2515.
- Q. Yao, Z. Wu, Z. Liu, Y. Lin, X. Yuan and J. Xie, *Chem. Sci.*, 2021, **12**, 99–127.
- S. Kolay, D. Bain, S. Maity, A. Devi, A. Patra and R. Antoine, *Nanomaterials*, 2022, **12**, 544.
- Y. Hong, J. W. Y. Lam and B. Z. Tang, *Chem. Commun.*, 2009, 4332.
- X. Jia, J. Li and E. Wang, *Small*, 2013, **9**, 3873–3879.

- 30 N. Goswami, Q. Yao, Z. Luo, J. Li, T. Chen and J. Xie, *J. Phys. Chem. Lett.*, 2016, **7**, 962–975.
- 31 Z. Wu, Q. Yao, S.-q. Zang and J. Xie, *Natl. Sci. Rev.*, 2021, **8**, nwaa208.
- 32 D. Bera and N. Goswami, *J. Phys. Chem. Lett.*, 2021, **12**, 9033–9046.
- 33 K. Sahoo and I. Chakraborty, *Nanoscale*, 2023, **15**, 3120–3129.
- 34 D. Bain, A. Devi, Rashi, S. Chakraborty, S. Kolay and A. Patra, *J. Phys. Chem. C*, 2023, **127**, 18244–18251.
- 35 Q. Yao, Z. Luo, X. Yuan, Y. Yu, C. Zhang, J. Xie and J. Y. Lee, *Sci. Rep.*, 2014, **4**, 3848.
- 36 B. Kuppam and U. Maitra, *Nanoscale*, 2017, **9**, 15494–15504.
- 37 Z.-C. Shen, Y.-T. Yang, Y.-Z. Guo, Y.-Q. Chai, J.-L. Liu and R. Yuan, *Anal. Chem.*, 2023, **95**, 5568–5574.
- 38 F. Qu, L. Zhao, W. Han and J. You, *J. Mater. Chem. B*, 2018, **6**, 4995–5002.
- 39 S. Chandra, Nonappa, G. Beaune, A. Som, S. Zhou, J. Lahtinen, H. Jiang, J. V. Timonen, O. Ikkala and R. H. Ras, *Adv. Opt. Mater.*, 2019, **7**, 1900620.
- 40 J. S. Mohanty, K. Chaudhari, C. Sudhakar and T. Pradeep, *J. Phys. Chem. C*, 2019, **123**, 28969–28976.
- 41 M. H. Chua, K. L. O. Chin, X. J. Loh, Q. Zhu and J. Xu, *ACS Nano*, 2023, **17**, 1845–1878.
- 42 J. Koivisto, X. Chen, S. Donnini, T. Lahtinen, H. Häkkinen, G. Groenhof and M. Pettersson, *J. Phys. Chem. C*, 2016, **120**, 10041–10050.
- 43 M. Invernizzi and M. Parrinello, *J. Phys. Chem. Lett.*, 2020, **11**, 2731–2736.
- 44 M. Invernizzi and M. Parrinello, *J. Chem. Theory Comput.*, 2022, **18**, 3988–3996.
- 45 J. Liu, X. Yang, K. Wang, X. He, Q. Wang, J. Huang and Y. Liu, *ACS Nano*, 2012, **6**, 4973–4983.
- 46 Q. Yao, L. Liu, S. Malola, M. Ge, H. Xu, Z. Wu, T. Chen, Y. Cao, M. F. Matus, A. Pihlajamäki, Y. Han, H. Häkkinen and J. Xie, *Nat. Chem.*, 2023, **15**, 230–239.
- 47 S. Franco-Ulloa, L. Riccardi, F. Rimembrana, M. Pini and M. De Vivo, *J. Chem. Theory Comput.*, 2019, **15**, 2022–2032.
- 48 S. Franco-Ulloa, L. Riccardi, F. Rimembrana, E. Grottin, M. Pini and M. De Vivo, *J. Chem. Theory Comput.*, 2023, **19**, 1582–1591.
- 49 E. Pohjolainen, X. Chen, S. Malola, G. Groenhof and H. Häkkinen, *J. Chem. Theory Comput.*, 2016, **12**, 1342–1350.
- 50 H. Heinz, R. A. Vaia, B. L. Farmer and R. R. Naik, *J. Phys. Chem. C*, 2008, **112**, 17281–17290.
- 51 J. Wang, R. M. Wolf, J. W. Caldwell, P. A. Kollman and D. A. Case, *J. Comput. Chem.*, 2004, **25**, 1157–1174.
- 52 A. S. de Araujo, M. T. Sonoda, O. E. Piro and E. E. Castellano, *J. Phys. Chem. B*, 2007, **111**, 2219–2224.
- 53 A. Barducci, G. Bussi and M. Parrinello, *Phys. Rev. Lett.*, 2008, **100**, 020603.